OPEN

NPG Asia Materials (2016) 8, e263; doi:10.1038/am.2016.46
www.nature.com/am

ORIGINAL ARTICLE

Layer-controlled growth of MoS_2 on self-assembled flower-like Bi_2S_3 for enhanced photocatalysis under visible light irradiation

Lu-Lu Long[1], Jie-Jie Chen[1], Xing Zhang[1], Ai-Yong Zhang[1,2], Yu-Xi Huang[1], Qing Rong[1] and Han-Qing Yu[1]

Metal sulfide semiconductors, such as molybdenum disulfide (MoS_2) and bismuth trisulphide (Bi_2S_3), are of considerable interest for their excellent applications in photocatalysis and in many other fields. However, the controllable synthesis of MoS_2/Bi_2S_3 hybrid nanostructures remains a challenge. In this study, we report a unique sacrificial templating strategy for preparing layer-controlled MoS_2 on three-dimensional (3D) Bi_2S_3 micro-flowers. For this approach, Bi_2S_3 was utilized as a sacrificial template to regulate the ion exchange, and the dosage of molybdenum was adjusted to tune the dynamic formation, thus converting the MoS_2 nanosheets on the Bi_2S_3 micro-flowers from monolayer to multilayer. Such a 3D flower-like hybrid nanostructure enables MoS_2/Bi_2S_3 to exhibit adsorption-promoted photocatalysis under visible light irradiation, especially for the excellent photodegradation of low-concentration organic pollutants, for example, azo dye and atrazine. The observed superiority of the 3D MoS_2/Bi_2S_3 was mainly attributed to the increased mass transfer, robust light-harvesting capacity, improved charge separation, lower oxygen-activation barrier and enhanced active oxygen yield. Our findings are of interest for the development of novel S-based photocatalysts and provide a new opportunity to efficiently remove low-concentration refractory pollutants.
NPG Asia Materials (2016) **8,** e263; doi:10.1038/am.2016.46; published online 15 April 2016

INTRODUCTION

In recent years, metal sulfide semiconductors have been developed for environmental photocatalysis because of their narrow bandgaps, high sunlight absorption and satisfactory catalytic activity.[1–4] Among them, Bi_2S_3 is a promising visible light-driven photocatalyst owing to its low toxicity and narrow direct band gap of ~1.3 eV.[5] However, Bi_2S_3 usually exhibits a substantially lower photocatalytic activity than expected, mainly because of severe charge recombination and structural photocorrosion.[4] To achieve good carrier separation, the construction of a built-in electric field (band bending) is usually required. One effective way to enhance band bending is to create a thermodynamically driven heterojunction by incorporating another semiconductor, depending on the favored band offsets between the two semiconductors.[6] Generally, the semiconductor that is incorporated as a cocatalyst to construct such a self-established heterojunction should possess good electric conductivity, a suitable energy structure and excellent electrochemical activity.[7–11]

As a typical layered metal sulfide, MoS_2 has drawn increasing attention because of its layered structure similar to that of graphene, which is composed of three atom layers stacked together through Van der Waals interactions.[12,13] Such a two-dimensional (2D) layered-crystal structure provides convenient electron transfer and many active sites for interfacial adsorption.[12,14] Moreover, the edge sites of MoS_2 nanosheets are generally recognized as the thermodynamically active sites for electrochemical hydrogen evolution.[15] As an important non-noble cocatalyst, MoS_2 is a highly promising candidate for photocatalysis and many other applications.[16–20] Thus, using MoS_2 is reasonable for strengthening the visible light photocatalytic performance of Bi_2S_3.[21–24]

As a cocatalyst, the morphology and nanostructure of MoS_2, for example, nanoparticles,[25] nanoclusters,[26] nanospheres[27] and nanosheets,[19,28] have considerable effects on the catalytic performance of MoS_2-activated hybrids. MoS_2 in the form of nanosheets usually exhibits much better catalytic performance due to its 2D layered structure with a larger surface area and more active sites than those of other nanostructures.[28] Furthermore, the layer of MoS_2 also governs its properties and performance, as both the active sites and adsorption ability are substantially influenced by the layered nanostructure.[28–30] Thus, constructing three-dimensional (3D) MoS_2 heterostructures with suitable layers for catalytic applications is a reasonable approach.[28,31,32] However, controlling the synthesis of MoS_2 nanosheets as a cocatalyst remains a serious challenge, and most of the available 3D heterostructures are prepared by two or more steps.[17,28,33,34] Hence, developing a simple, controllable general approach to synthesize 3D MoS_2-based heterostructures is of considerable interest for cocatalyst applications.

[1]Department of Chemistry, CAS Key Laboratory of Urban Pollutant Conversion, University of Science and Technology of China, Hefei, China and [2]Department of Municipal Engineering, Hefei University of Technology, Hefei, China
Correspondence: Dr A-Y Zhang or Professor H-Q Yu, Department of Chemistry, CAS Key Laboratory of Urban Pollutant Conversion, University of Science and Technology of China, Jinzhai Road 96, Hefei 230026, China.
E-mail: aiyzhang@ustc.edu.cn or hqyu@ustc.edu.cn
Received 25 October 2015; revised 23 January 2016; accepted 16 February 2016

Herein, we report a simple general sacrificial template method to effectively regulate both the nanostructure of a MoS_2 cocatalyst and the properties and catalytic performance of a novel 3D MoS_2/Bi_2S_3 hybrid. The number of MoS_2 layers could be simply and effectively regulated via this one-pot hydrothermal process based on an ion-exchange mechanism. In this approach, Bi_2S_3 was first generated and then acted as a sacrificial template for the subsequent MoS_2 nanosheet growth from a monolayer to multiple layers. Moreover, a favorable 3D nanostructure could be effectively constructed when the number of MoS_2 layers was regulated properly. To test an application, two typical organic pollutants, azo dye and atrazine, were degraded on this 3D MoS_2/Bi_2S_3 hybrid under visible light irradiation.

MATERIALS AND METHODS

Reagents and materials

All chemicals were reagent grade and used as received without further purification. $Bi(NO_3)_3{\cdot}5H_2O$, azo dye and atrazine were purchased from Aladdin Reagent (Shanghai, China). Sulfourea and sodium molybdate were purchased from Shanghai Reagent (Shanghai, China). The polycrystalline TiO_2 P25 (Degussa, Frankfurt, Germany) had a mean particle size of ~25 nm, an anatase/rutile ratio of 80:20 and a specific surface area of ~50 $m^2\,g^{-1}$. High-purity deionized water was used in this study.

One-pot synthesis of 3D MoS_2/Bi_2S_3

First, 30 mg of $Bi(NO_3)_3{\cdot}5H_2O$ was dissolved in deionized water, and then, a defined dosage of Na_2MoO_4 and an excess of sulfourea (70 mg) were added to this solution. The total volume of the solution was fixed at 20 ml. The solution was transferred into a Teflon-lined stainless steel autoclave, which contained a suitably sized clean plate substrate, that is, carbon paper or glass, placed against the wall. The hydrothermal process was carried out at 200 °C for 24h. Then, the black flower-like 3D MoS_2/Bi_2S_3 was collected from the plate substrate by sonication and centrifugation. Finally, the collected samples were washed repeatedly with deionized water and dried at 60 °C for 12h. The samples prepared with Na_2MoO_4 dosages of 5, 10, 15, 30 and 60 mg were designated as MoBi-5, MoBi-10, MoBi-15, MoBi-30 and MoBi-60, respectively.

For comparison, bare Bi_2S_3 was prepared by the same procedure without the addition of Na_2MoO_4, whereas bare MoS_2 was prepared by the same procedure without the addition of $Bi(NO_3)_3{\cdot}5H_2O$.

Characterization

The morphology and structure of the samples were characterized using a field-emission scanning electron microscope (SIRION200; FEI, Eindhoven, The Netherlands). Transmission electron imaging selected-area electron diffraction was performed on a high-resolution transmission electron microscope (TEM-JEM-ARM200F; JEOL, Tokyo, Japan). The chemical compositions of the samples were characterized by an energy dispersive X-ray analyzer (GENESIS; EDAX, Mahwah, NJ, USA) fitted to the TEM chamber. X-ray diffraction (XRD) was carried out using an X'celerator detector (X'pert PANalytical BV, Almelo, The Netherlands). X-ray photoelectron spectroscopy was performed using an ESCALAB250 (Thermo Fisher, San Jose, CA, USA). The diffuse reflectance spectra were measured using a UV/Vis spectrophotometer (UV 2550; Shimadzu, Tokyo, Japan). The surface area was measured by the Brunauer–Emmett–Teller method with a Builder 4200 instrument (Tristar II 3020M; Micromeritics, Norcross, GA, USA) in liquid nitrogen. The working electrode was prepared by using dip-coating technology (photocatalyst: 1.0 $g\,l^{-1}$). Electrochemical impedance spectroscopy was measured by applying an AC voltage with an amplitude of −0.33 V (versus Ag/AgCl) within a frequency range from 10^5 to 10^{-1} Hz in a 0.2 M $Na_2S{\cdot}9H_2O$ aqueous solution. The photocurrent was measured at 0.25 V (versus Ag/AgCl) in 0.1 M Na_2SO_4 aqueous solution. The oxygen reduction reaction tests were conducted in 0.1 M KOH solution with a rotating-disk electrode (Pine Research Instrumentation, Grove, PA, USA). Mott–Schottky plots were obtained using impedance measurements at a fixed frequency of 1000 Hz in an applied voltage range of −0.50 to 1.0 V in 0.1 M Na_2SO_4 aqueous solution (pH = ~7.0). All electrochemical tests were conducted in a three-electrode electrochemical system using a CHI660 potentiostat (Chenhua, Shanghai, China), and a saturated Ag/AgCl (3.0 M KCl) was used as the reference electrode, with a standard potential of 0.197 V versus a normal hydrogen electrode (NHE). The fluorescence tests were conducted in a custom-built photoreactor with an effective volume of 60 ml. The light source was a 500 W Xe arc lamp (PLS-SXE500; Trusttech, Beijing, China), with a 10 cm infrared water filter and a Pyrex filter ($\lambda > 420$ nm). For each test, 50 ml of aqueous solution containing 0.1 $g\,l^{-1}$ catalyst, 1 mM terephthalic acid and 0.01 M NaOH were used. Fluorescence spectra were recorded using a spectrofluorophotometer (RF-5301PC; Shimadzu). The ESR signal spin-trapped by 5,5-dimethyl-pyrroline-N-oxide was recorded on a Bruker spectrometer (A300, Bruker, Karlsruhe, Germany) with the following settings: center field = 3512 G, microwave frequency = 9.86 GHz and power = 6.36 mW. The water contact angle was measured with a contact angle analyzer (JC2000A; Powereach, Beijing, China). The zeta potential analysis was performed on a Zetasizer (Nano-Z; Malvern, Worcester, UK), in a folded capillary cell (DTS1060) made from polycarbonate with gold-plated beryllium/copper electrodes.

Photocatalytic degradation tests

The photocatalytic activity of 3D MoS_2/Bi_2S_3 was evaluated by the degradation of rhodamine B (RhB) and atrazine under visible light irradiation, with 0.15 M Na_2SO_3 and 0.1 M Na_2S as sacrificial reagents. A 500 W xenon arc lamp equipped with a pass filter ($\lambda > 420$ nm) was used as a simulated light source. For the RhB degradation, 4 mg of MoS_2/Bi_2S_3 was dispersed into 20 ml RhB aqueous solution (5 $mg\,l^{-1}$), whereas for the atrazine degradation, 30 mg of the photocatalyst was dosed into 60 ml atrazine solution (5 $mg\,l^{-1}$). Before irradiation, the solution was sonicated for 10 min and then stirred for 20 min. During the reaction, 1-ml aliquots were sampled regularly. The amounts of RhB and atrazine in the aliquots were analyzed using a UV-visible spectrophotometer (UV-2401PC, Shimadzu) and high-performance liquid chromatography (1100; Agilent, Palo Alto, CA, USA), respectively, with a variable-wavelength detector set at 220 nm. The mobile phase consisted of H_2O and methanol (50:50), and the flow rate was 0.8 ml min^{-1}. The total organic carbon was measured by a total organic carbon analyzer (Multi N/C 2100; Analytik Jena, Jena, Germany).

RESULTS AND DISCUSSION

Morphology and structure of 3D MoS_2/Bi_2S_3

The prepared Bi_2S_3 with the micro-flower morphology was self-assembled from micro-rods with a length of 2–3 μm and a width of 200–400 nm (Supplementary Figure S1a). Figures 1a–c shows typical SEM images of 3D MoS_2/Bi_2S_3 (MoBi-30) at low and high magnifications, in which most of the Bi_2S_3 micro-flowers were uniformly covered by MoS_2 nanosheets. A large number of MoS_2 nanosheets were directly grown on each micro-rod of the Bi_2S_3 micro-flowers, forming the 3D flower-like heterostructure (Figure 1d). The shell thickness and the core diameter were identified to be ~50 and ~100 nm, respectively. During the hydrothermal growth, Bi_2S_3 could act as the sacrificial template to provide active sites for MoS_2 growth. In the absence of the Bi_2S_3 template, the MoS_2 nanosheets similarly self-assembled to form flower-like microspheres (Supplementary Figures S1b–f).

The crystal structure of the 3D MoS_2/Bi_2S_3 heterostructures was further investigated by XRD (Supplementary Figure S2a). The diffraction peaks of the MoS_2 nanosheets corresponded well to the standard peaks of the MoS_2 hexagonal phase (JCPDS card No. 37–1492; Supplementary Figure S2b), and the diffraction peaks of Bi_2S_3 could be indexed to the crystalline planes of the Bi_2S_3 orthorhombic phase (JCPDS card No. 17–0320; Supplementary Figure S2c). Moreover, all the diffraction peaks of these two semiconductors were simultaneously observed in the XRD pattern of 3D MoS_2/Bi_2S_3.

In addition, 3D MoS_2/Bi_2S_3 (MoBi-30) was further observed by high-resolution TEM. The MoS_2 nanoflakes and the Bi_2S_3 micro-rods

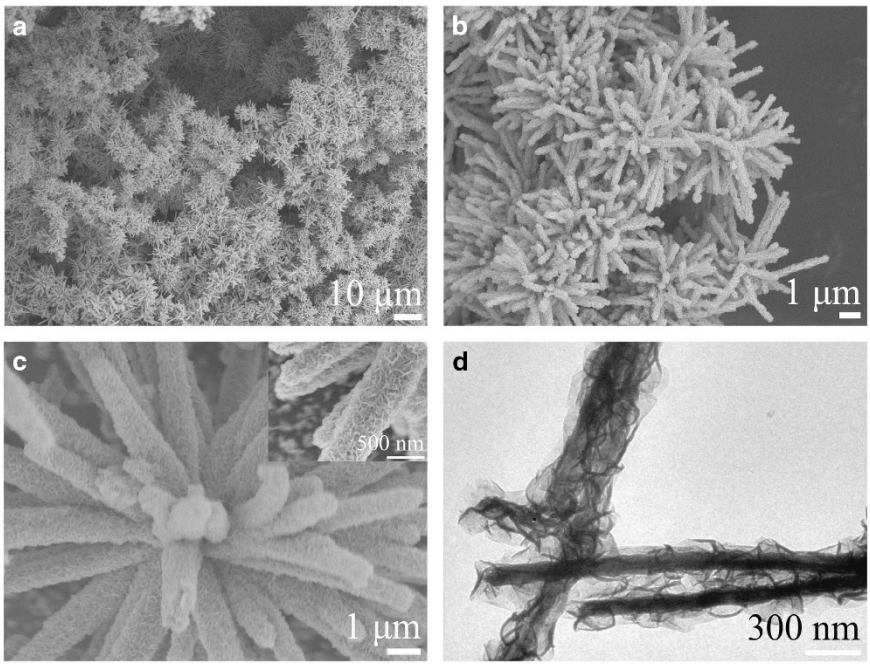

Figure 1 Scanning electron microscope (SEM) (**a**–**c**) and transmission electron microscope (TEM) (**d**) images of 3D MoS_2/Bi_2S_3 (MoBi-30).

were densely interconnected (Figure 2a). The selected-area electron diffraction patterns (Figure 2a, inset) indicated two-component crystalline characteristics: one set of spots was indexed to single crystalline Bi_2S_3 micro-rods, and another set of rings was attributed to the MoS_2 nanosheets, arising from the stacking of MoS_2 nanosheets with different crystallographic orientations. Furthermore, the high-resolution TEM images of the Bi_2S_3 micro-rods (Figure 2b), MoS_2 nanosheets (Figure 2c) together with the selected-area electron diffraction patterns further confirm the crystal structure of the 3D MoS_2/Bi_2S_3. The inter-plane spacings of 0.80 and 0.39 nm could be assigned to the (110) and (001) planes of the orthorhombic Bi_2S_3, respectively. The fringes with lattice spacings of 0.27 and 0.57 nm corresponded to the (100) and (002) planes of MoS_2, respectively. The characteristic peak of the (002) crystalline plane at 14.2° in the XRD pattern suggests the ordered stacking of S-Mo-S layers (Figure 2d). At least ten layers of MoS_2 nanosheets grew on the Bi_2S_3 micro-rods. The high-resolution TEM observations indicate that Bi_2S_3 nanorods grew along the [001] crystallographic direction with the (110) surface as the outside surface, in contact with the (001) surface of MoS_2.

The crystal surface matching of the Bi_2S_3 and MoS_2 could be explained at the atomic level by the structural model of the MoS_2/Bi_2S_3. The Bi_2S_3 nanorod could be constructed from the Bi_2S_3 crystal based on the (110) plane. The XRD results show that the crystal structures of Bi_2S_3 and MoS_2 in this heterostructure each belonged to orthorhombic and hexagonal crystal systems, respectively, corresponding to the space groups of Pbnm and P63/mmc, respectively. The crystal cells of orthorhombic Bi_2S_3 and hexagonal MoS_2 are shown in Supplementary Figures S3a and b. Then, the (110) surface of the Bi_2S_3 and the (001) surface of MoS_2 were cleaved from the crystal structures. The distance between adjacent Bi atoms exposed on the (110) crystal surface of orthorhombic Bi_2S_3 was 15.864 Å, and S atoms appeared at 3.168 Å intervals along the (001) surface of hexagonal MoS_2 (Figure 2e). Thus, five intervals (15.840 Å) of the S–S distance on the (001) surface of the MoS_2 nanosheet matched well with the Bi–Bi distance on the outside surface of the Bi_2S_3 nanorod (Figure 2e). This might be beneficial for the growth of the MoS_2 nanosheet on the Bi_2S_3 nanorod via the interaction of S and Bi atoms to form the heterostructure. The high-resolution TEM image and energy dispersive X-ray mappings (Figures 2f–i) provide more evidence for the combination of MoS_2 nanosheets and Bi_2S_3 micro-rods. A Bi_2S_3 micro-rod was located in the center of the 3D heterostructure, whereas MoS_2 nanosheets were homogeneously distributed over the whole micro-rod. A uniform distribution of Bi, Mo and S throughout the 3D MoS_2/Bi_2S_3 was clearly observed (Figures 2f–i), with an atomic ratio of 11.63:29.49:58.89 (Supplementary Figure S4). The surface composition and chemical states of the heterostructures were characterized, and the results confirmed the successful growth of MoS_2 and Bi_2S_3 (Supplementary Figure S5), which agrees well with the XRD results (Supplementary Figure S2). Moreover, both Mo 3D high-resolution X-ray photoelectron spectroscopy spectra could be fitted to the two components associated with the 1T and 2H phases,[15,18,21] indicating the co-existence of these two polymorphs (Supplementary Figures S5c,i). In addition, much lower surface areas were obtained for both bare Bi_2S_3 and MoS_2, that is, 1.67 and 5.94 $m^2 g^{-1}$, respectively. This was attributed mainly to either the low-dimensional morphology or the much larger apparent thickness of the nanosheets and their severe aggregation (Supplementary Figures S1b–f)[25,35] compared with 3D MoS_2/Bi_2S_3 (25.65 $m^2 g^{-1}$, Supplementary Figure S6).

Formation mechanism of 3D MoS_2/Bi_2S_3

As the SEM images of the transitional structures with increasing reaction times provide more direct evidence (Supplementary Figure S7), the cation-exchange formation mechanism of the 3D MoS_2/Bi_2S_3 micro-flowers is proposed (Figure 3). In the first step, randomly packed amorphous Bi_2S_3 nanowires were initially generated as a precursor, while MoO_4^{2-} and sulfur released by sulfourea were distributed around the Bi_2S_3 nanowires, and a small amount of MoS_2 nanosheet subunits appeared as a scaffold on the surface of the Bi_2S_3 nanowires (Supplementary Figures S7a–d, 4–12h); Bi_2S_3 nanowires further grew into micro-rods, and the MoS_2 nanosheets became much

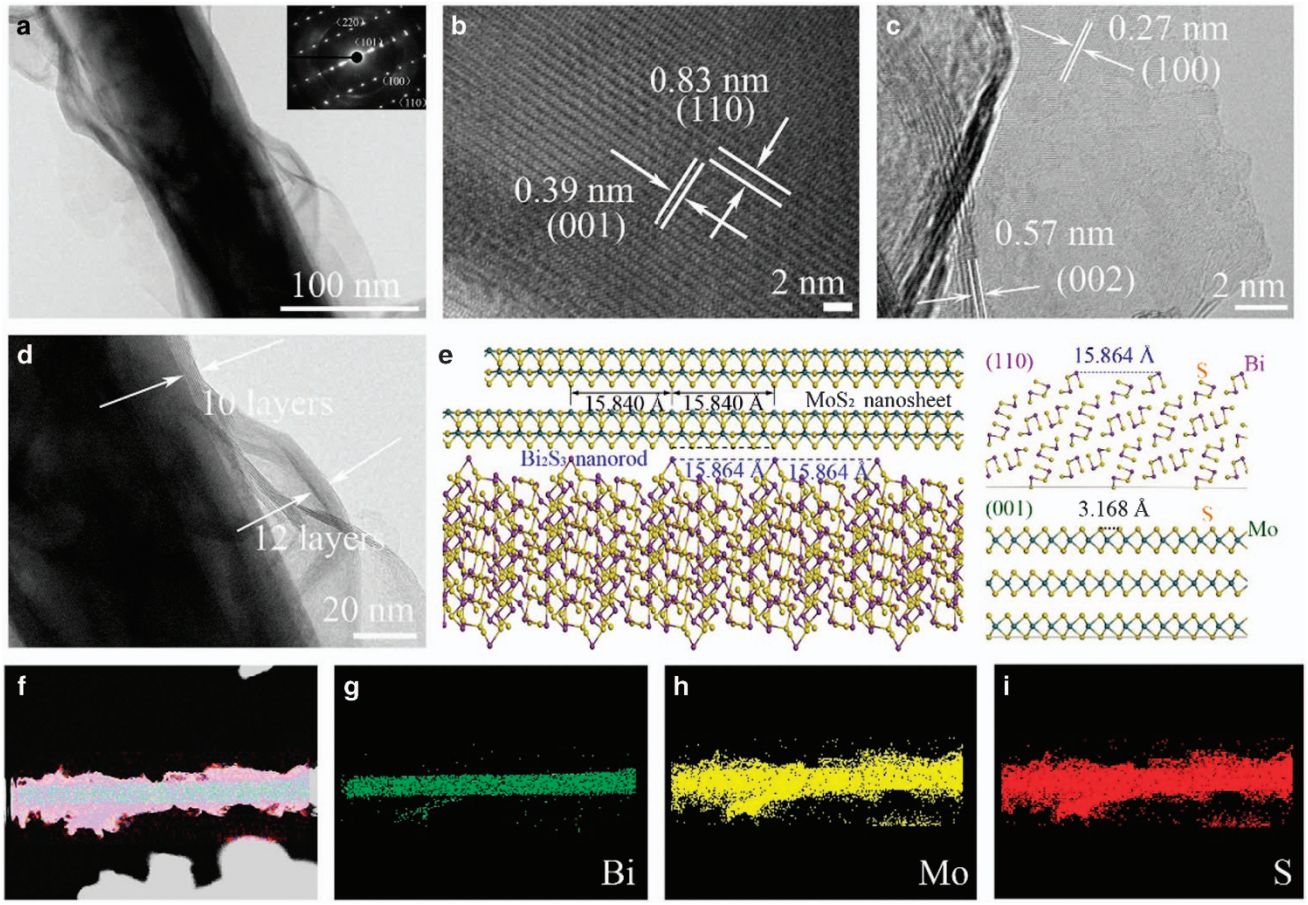

Figure 2 Transmission electron microscope (TEM) (**a**, **d**) and high-resolution transmission electron microscope (HRTEM) (**b**, **c**) images of 3D MoS_2/Bi_2S_3 (MoBi-30), the inset of **a** is its selected-area electron diffraction (SAED) pattern, and the thickness of one MoS_2 layer is ~0.6 nm; crystal surface match between the (001) surface of the MoS_2 nanosheet and the outside surface of the Bi_2S_3 nanorod, the (110) surface of orthorhombic Bi_2S_3 with the distance (15.864 Å) between adjacent Bi atoms and the (001) surface cleaved from hexagonal MoS_2, the S atom appears at the intervals of 3.168 Å (**e**); STEM image and the energy dispersive X-ray (EDX) elemental mappings of Bi, Mo and S (**f**–**i**).

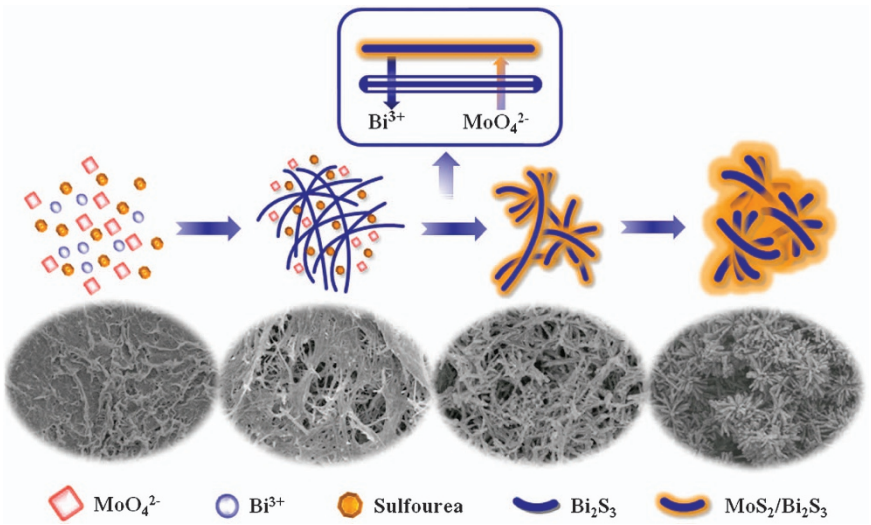

Figure 3 Formation of 3D MoS_2/Bi_2S_3 via a cation-exchange mechanism.

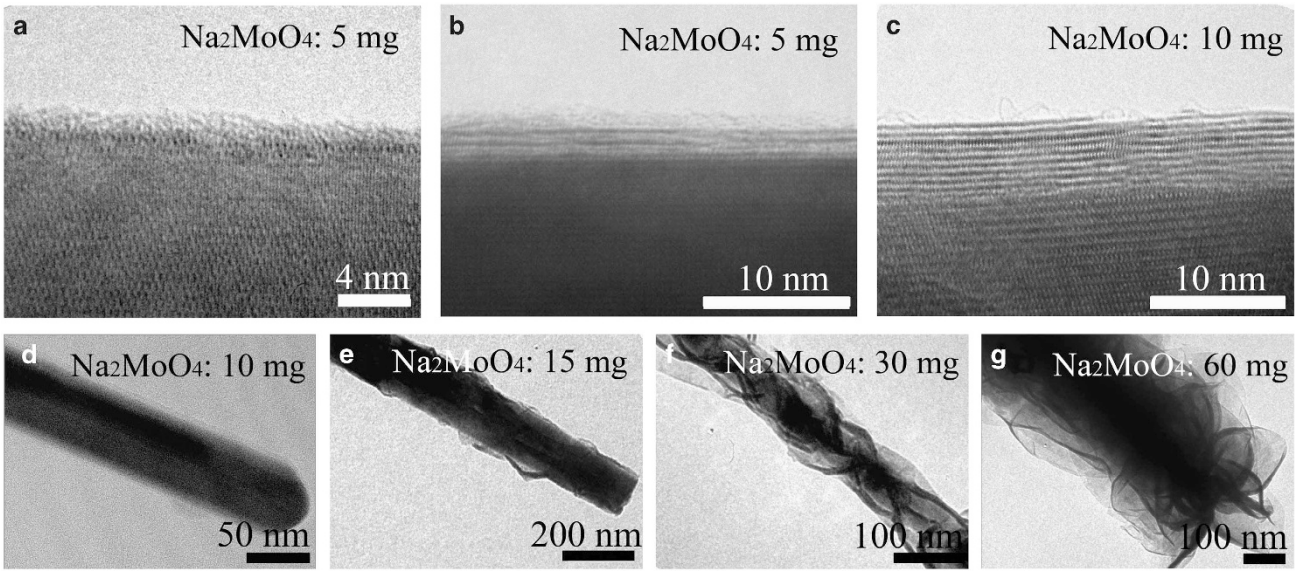

Figure 4 High-resolution transmission electron microscope (HRTEM) and transmission electron microscope (TEM) images of 3D MoS_2/Bi_2S_3 hybrid with different layers of MoS_2 nanosheets: MoBi-5 (**a**, **b**), MoBi-10 (**c**, **d**), MoBi-15 (**e**), MoBi-30 (**f**) and MoBi-60 (**g**).

thicker as the reaction progressed (Supplementary Figure S7e, 16h). Then, Bi_2S_3 nanowires continuously became increasingly thicker and started to overlap each other, ultimately self-assembling into 3D MoS_2/Bi_2S_3 micro-flowers, which were comprised of Bi_2S_3 micro-rods uniformly coated by the layer-controlled MoS_2 nanosheets (Supplementary Figure S7f, 24h). With the increasing hydrothermal time, the thickness of the MoS_2 layer progressively increased, and the Bi_2S_3 nanorods became increasingly thinner (Supplementary Figure S7g, 27h). When the hydrothermal time was prolonged to 30h, Bi_2S_3 nanorods almost completely disappeared, and the thickness of MoS_2 layer peaked (Supplementary Figures S7h,i). These SEM images provide solid evidence that the as-formed Bi_2S_3 acted as a sacrificial template for the subsequent MoS_2 growth and the final formation of the 3D MoS_2/Bi_2S_3 hybrid.

The XRD results further validate the SEM observations (Supplementary Figure S8). The XRD pattern of the sample isolated at 6h clearly shows weak diffraction peaks, which are coincident with the orthorhombic phase of Bi_2S_3 (JCPDS 17–0320). This indicates its primary formation as a sacrificial precursor at the initial stage of the hydrothermal process. In comparison, no diffraction peaks assigned to MoS_2 were detected, which might be mainly due to its small dosage and/or high dispersity. After the reaction time was increased to 12h, the intensity of the Bi_2S_3 diffraction peaks substantially increased, and the characteristic XRD peak for the hexagonal phase of MoS_2 positioned at $\sim 14.0°$ could be clearly detected (JCPDS 37–1492), indicating the continuous growth of both Bi_2S_3 and MoS_2. The intensity of the diffraction peaks of Bi_2S_3 peaked at 16h then progressively decreased with the continuous increase in the MoS_2 dosage. When the hydrothermal process was further prolonged to 30h, the intensity of the MoS_2 diffraction peaks reached a maximum, whereas the diffraction peaks for the orthorhombic phase of Bi_2S_3 became considerably weaker, as in the first 6h of the reaction, which should mainly be attributed to the substantial increase in the dosage of MoS_2 nanosheets locally grown on the surface of Bi_2S_3 nanorods. These time-dependent phase structures shown by the XRD results agree well with the time-dependent morphologies from the SEM images (Supplementary Figure S7).

Furthermore, the TEM images that were isolated from the reaction mixture at 16–30h also provide direct proof for the cation-exchange formation mechanism of the 3D MoS_2/Bi_2S_3 hybrid (Supplementary Figure S9). When the hydrothermal time was prolonged from 16 to 30h, the thickness of MoS_2 layer progressively increased, and the Bi_2S_3 nanowires continuously became increasingly thinner (Supplementary Figures S9a–c, 16–27h). When the hydrothermal time was further prolonged to 30h, Bi_2S_3 almost completely disappeared, and the thickness of the MoS_2 layer reached its maximum value (Supplementary Figure S9d). The TEM images of the transitional structures isolated at different reaction times further prove that the 3D MoS_2/Bi_2S_3 hybrid formed using Bi_2S_3 nanorods as a sacrificial template for localized MoS_2 growth via the cation-exchange mechanism. After 30h of hydrothermal reaction, most of the Bi_2S_3 nanowires were converted into MoS_2 under the driving force of the solubility difference in aqueous solution.

Although the solubility of Bi_2S_3 in aqueous solution is much lower than MoS_2 with K_{sp} values of 1.0×10^{-97} and 2.2×10^{-56}, respectively,[36] MoS_2 nanosheets were formed by utilizing Bi_2S_3 nanorods as a sacrificial precursor, as illustrated by the SEM, TEM and XRD results (Figures 1,2 and 4 and Supplementary Figures S7). The MoS_2 nanosheets grew with the sulfur from the as-formed Bi_2S_3 nanorods, rather than with an auxiliary source from the reaction solution, that is, thiourea. The main reason for such an unexpected structural transition from the low-solubility Bi_2S_3 to the high-solubility MoS_2 might mainly be attributed to the strong complexing between the added thiourea, a typical organic complexing agent, and the lattice bismuth species in the Bi_2S_3 nanorods, as in the spectrophotometric determination of bismuth ($Bi^{3+}+CS(NH_2)_2 \rightarrow (BiCS(NH_2)_2)^{3+}$, number of ligands = 6, $\lg\beta_n = 11.9$).[37,38] From the standpoint of crystal growth, the presence of thiourea sufficiently facilitated the lattice ≡Bi(III) release from the crystal structure of the Bi_2S_3 nanorods, which served as a unique substrate, rather than as a typical catalyst for the subsequent MoS_2 formation. This favored the strong thiourea complexation of Bi^{3+} on the surface of the Bi_2S_3 nanorods, and could be anticipated to shift the reaction equilibrium toward MoS_2 formation by recombining the liberated sulfur species from the Bi_2S_3 nanorods with the molybdenum species from the aqueous solution, MoO_4^{2-}

and therefore to change the thermodynamic balance between the K_{sp} of Bi_2S_3 and MoS_2, as mentioned above. Similar results have been previously reported.[39,40] Moreover, in addition to Bi_2S_3, another composite, that is, Sb_2S_3, could also act as a template for the controllable growth of MoS_2 nanosheets (Supplementary Figure S10). As a result, the developed method using a sacrificial template might be used as a general way to synthesize MoS_2 nanosheet-based hybrid.

The layers of MoS_2 nanosheets on the Bi_2S_3 micro-rods and in the 3D MoS_2/Bi_2S_3 heterostructure could be effectively regulated by controlling the dosage of Na_2MoO_4 added to the hydrothermal reaction (Figure 4). When a small amount (that is, 5 mg) of Na_2MoO_4 was added, amorphous MoS_2 or monolayer MoS_2 grew on the surface of the Bi_2S_3 nanorods (Figures 4a and b). By increasing the dosage of Na_2MoO_4 to 15 mg, the number of MoS_2 layers on the Bi_2S_3 nanorods could be substantially increased (Figures 4c–e and Supplementary Figure S11a). At an adequate dosage of Na_2MoO_4, that is, 30 mg, the MoS_2 film could be sufficiently thick, and the morphology of 3D MoS_2/Bi_2S_3 was well-defined (Figure 4f). An excessive dose of Na_2MoO_4, that is, 60 mg, resulted in the much thicker and more densely grown MoS_2 nanosheets with decreased inter-spaces (Figure 4g and Supplementary Figure S11b). These results clearly indicate that the dosage of added Na_2MoO_4 had a dominant role in controlling the layers of MoS_2 nanosheets locally grown on the Bi_2S_3 surface.

Adsorption-promoted degradation of low-concentration refractory pollutants by 3D MoS_2/Bi_2S_3

For the photocatalytic degradation of refractory pollutants, the overall rate resistance should be the summation of the mass-transfer resistance and the chemical reaction resistance. Thus, both the adsorption capacity and the catalytic activity are the two factors that equally govern efficient photocatalysis. As shown in Figure 5a, the MoS_2 with a 2D layered structure exhibited an almost two times higher RhB adsorption capacity than that of the Bi_2S_3 analog under identical conditions, indicating that anchoring MoS_2 onto Bi_2S_3 could significantly enhance its adsorption capacity for subsequent catalytic reactions. However, because of the severe aggregation and the low specific surface area of the self-assembled MoS_2 flower-like microspheres (Supplementary Figures S1b–f),[25,35] its RhB adsorption capacity (37 mg g^{-1}) was substantially smaller than that of 3D MoS_2/Bi_2S_3 (50 mg g^{-1}; Supplementary Figures S12a–c), although less MoS_2 mass was present in the hybrid. Furthermore, RhB might be adsorbed by van der Waals or π–π interactions and hydrogen bonding rather than electrostatic forces,[41] despite the negatively charged surface of the photocatalysts at the given pH of 3.95–5.68 (Supplementary Figures S13a and b).

For the 3D MoS_2/Bi_2S_3, the MoBi-30 exhibited the largest adsorption capacity for low-concentration RhB and thus the highest removal efficiency for both the adsorption and degradation processes (Figure 5a). The 3D MoBi-30 had the highest specific surface area of 25.65 m^2 g^{-1} (Supplementary Figure S6), which might be due to the dense, outstretched and ultrathin well-defined plate-like morphology of the MoS_2 nanosheets and the sufficient inter-space of the Bi_2S_3 micro-flowers self-assembled by 1D micro-rods (Figure 1). For comparison, the physically mixed Bi_2S_3 micro-flowers and MoS_2 nanosheets (BiMo Mixed in Figure 5a) showed a much lower adsorption efficiency because of their loose and aggregated structure of MoS_2 and Bi_2S_3. This is further proven by the control experiments with MoS_2 nanosheets with either inadequate or excessive layers.

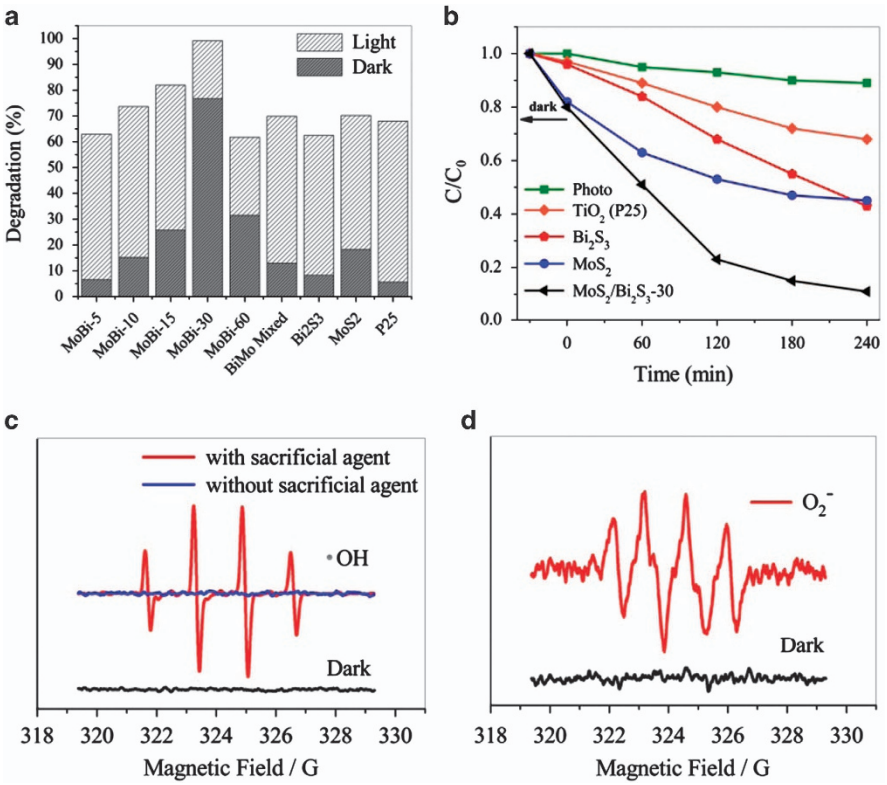

Figure 5 Photocatalytic degradation of rhodamine B (RhB) and atrazine by different photocatalysts (**a**, **b**); ESR signals of the 5,5-dimethyl-pyrroline-N-oxide (DMPO)-trapped •OH and DMPO-trapped $\bullet O_2^-$ on the 3D MoS_2/Bi_2S_3 (MoBi-30) under visible light and in the dark in the presence or absence of S^{2-}/SO_3^{2-} as a sacrificial agent (**c**, **d**).

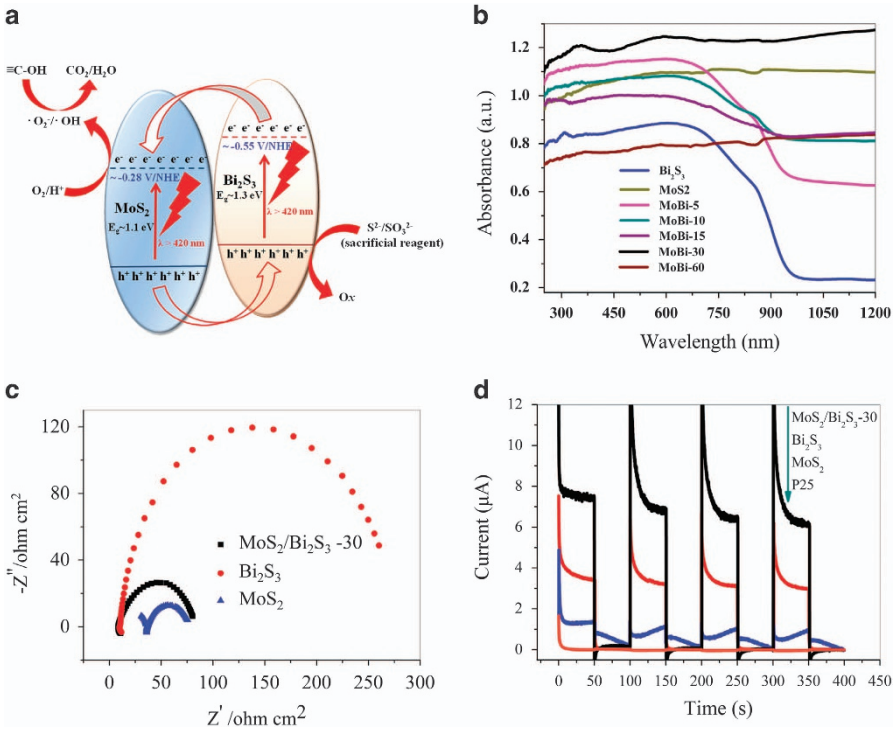

Figure 6 Photocatalytic mechanism of 3D MoS_2/Bi_2S_3 under visible light irradiation (**a**); diffuse reflectance spectra (DRS) of MoS_2, Bi_2S_3 and 3D MoS_2/Bi_2S_3 with different layers of MoS_2 nanosheets (**b**); electrochemical impedance spectroscopy (EIS) of MoS_2, Bi_2S_3 and 3D MoS_2/Bi_2S_3 (MoBi-30) at an open-circuit potential of −0.33 V (versus Ag/AgCl) (**c**); photocurrent of MoS_2, Bi_2S_3, 3D MoS_2/Bi_2S_3 (MoBi-30) and P25 under visible light irradiation at an external bias of +0.25 V (versus Ag/AgCl) (**d**).

The samples with few MoS_2 layers (MoBi-5, -10 and -15) showed a reduced ability to adsorb RhB with the decreasing layer of MoS_2 nanosheets, whereas the excessive MoS_2 nanosheets substantially damaged the 3D structure of the Bi_2S_3 micro-flowers, MoBi-60, by filling the inter-spaces between micro-rods. In addition, the overall RhB removal efficiency of BiMo-30 was considerably higher than that of Bi_2S_3, MoS_2 and commercial P25 (Figure 5a), which should mainly be attributed to the excellent adsorption capacity of the 3D MoS_2/Bi_2S_3.

Moreover, the excellent catalytic activity of the 3D MoS_2/Bi_2S_3 could be further proven by the adsorption-promoted photocatalytic degradation of atrazine, a typical herbicide widely present in water. After 240 min of irradiation, the highest removal efficiency of 89% was obtained by the 3D MoS_2/Bi_2S_3 (MoBi-30; Figure 5b), that is, higher than the results of some typical visible photocatalysts (Supplementary Figure S14).[42–44] The 3D MoS_2/Bi_2S_3 (MoBi-30) exhibited not only the largest adsorption capacity, but also the highest catalytic activity for atrazine degradation under visible light irradiation. Apparently, its high catalytic activity should be attributed to the strong synergistic effects between the good interfacial mass transfer and the rapid surface chemical reaction. In addition, atrazine might be dominantly adsorbed in its molecular form onto the negatively charged photocatalyst surfaces at the given pH (Supplementary Figure S13c).[45] Furthermore, its photocatalytic activity remained high after five cycles (Supplementary Figure S15), suggesting its good photocatalytic stability. The observed partial activity loss might be due to incomplete photocatalyst collection, organic surface deactivation and decreased adsorption capacity.[46]

The active species from 3D MoS_2/Bi_2S_3 in the photocatalytic degradation of atrazine were investigated by conducting ESR and radical inhibition tests. As shown in Figure 5c, the ESR spectra generated from 5,5-dimethyl-pyrroline-N-oxide-·OH adduct with a characteristic 1:2:2:1 pattern was measured in the 3D MoS_2/Bi_2S_3 aqueous solution with S^{2-}/SO_3^{2-} as a sacrificial agent. In comparison, no ESR spectra were observed in the absence of S^{2-}/SO_3^{2-}. This result should mainly be attributed to the rapid recombination of photo-excited electron-hole pairs with weak redox potentials. For $\cdot O_2^-$, the ESR spectra generated from the 5,5-dimethyl-pyrroline-N-oxide-$\cdot O_2^-$ adduct with a characteristic 1:1:1:1 pattern were measured only in the 3D MoS_2/Bi_2S_3 methanol solution in the presence of S^{2-}/SO_3^{2-} (Figure 5d). These results indicate that both ·OH and $\cdot O_2^-$ have important roles in the photocatalytic degradation of atrazine on the 3D MoS_2/Bi_2S_3 under visible light irradiation. In addition, the active species were further explored in the radical inhibition tests, in which S^{2-}/SO_3^{2-}, benzoquinone and tert-butyl alcohol were used as scavengers for photo-generated holes, $\cdot O_2^-$ and ·OH, respectively. Subtracting the contribution of dark adsorption, the net efficiency of removing atrazine by photocatalytic degradation was substantially improved from 15 to 70% (total organic carbon removal of 38.7%) when the photo-generated holes were captured (Supplementary Figure S16). However, the inhibition of either ·OH or $\cdot O_2^-$ considerably decreased the net atrazine removal efficiency from 70% to $<10\%$. These results are consistent with the ESR studies (Figures 5c and d) and further indicate that both ·OH and $\cdot O_2^-$ were the main active species for atrazine degradation by the 3D MoS_2/Bi_2S_3.

Photocatalytic mechanism of 3D MoS_2/Bi_2S_3

The photocatalytic mechanism of the 3D MoS_2/Bi_2S_3 hybrid under visible light irradiation is tentatively proposed (Figure 6a). To elucidate this mechanism, the energy structures of both Bi_2S_3 and MoS_2 were first studied to explore the separation, transfer and utilization properties of electron-hole pairs in the 3D MoS_2/Bi_2S_3. For Bi_2S_3, the band

gap energy was determined to be ~1.30 eV from its diffuse reflectance spectra spectrum by the Tauc equation (Supplementary Figures S17a and 6b), and its conduction band potential was measured to be ~−0.55 V/NHE (Supplementary Figure S17c). Similarly, MoS_2 is a narrow band gap semiconductor with a gap energy determined to be ~1.10 eV (Supplementary Figure S17b), and its conduction band potential was measured to be ~−0.28 V/NHE (Supplementary Figure S17d). The measured conduction band potential of Bi_2S_3 was sufficiently more negative than that of MoS_2, and thus, a typical type-II band gap alignment could be constructed between Bi_2S_3 and MoS_2 within the 3D MoS_2/Bi_2S_3 (Figure 6a), according to the Anderson model. With this mechanism, the photo-generated electrons in Bi_2S_3 under visible light irradiation were anticipated to be transferred to MoS_2, and a very enhanced separation, transfer and utilization efficiency of photocarriers was expected (reactions 1 and 2). The collected holes were consumed by S^{2-}/SO_3^{2-}, whereas the collected electrons reacted with the absorbed oxygen molecules on the MoS_2 surface to generate $\cdot O_2^-$ (reaction 3), which could further react with the surface-adsorbed protons to quickly produce ·OH to degrade the pollutants (Figure 6a; reactions 4 and 5). The enhanced oxygen reduction capacity of MoS_2 and the better hydrophilic property of 3D MoS_2/Bi_2S_3 favored the generation of both $\cdot O_2^-$ and ·OH (Supplementary Figures S18 and S19).[47]

$$MoS_2/Bi_2S_3 + h\nu \rightarrow MoS_2(e^- + h^+)/Bi_2S_3(e^- + h^+) \quad (1)$$

$$MoS_2(e^- + h^+)/Bi_2S_3(e^- + h^+) \rightarrow MoS_2(e^-)/Bi_2S_3(h^+) \quad (2)$$

$$MoS_2(e^-)/Bi_2S_3(h^+) + O_2 \rightarrow \cdot O_2^- \quad (3)$$

$$MoS_2(e^-)/Bi_2S_3(h^+) + O_2 + 2H^+ \rightarrow H_2O_2 \quad (4)$$

$$\cdot O_2^- + H_2O_2 \rightarrow OH + \cdot OH^- + O_2 \quad (5)$$

To explore the observed high catalytic activity of 3D MoS_2/Bi_2S_3, its optical properties were evaluated. The diffuse reflectance spectra of the 3D MoS_2/Bi_2S_3 showed a wide absorption band covering a broader visible light region (Figure 6b) owing to the intrinsic bandgaps of both Bi_2S_3 and MoS_2. After the MoS_2 nanosheets grew locally on the Bi_2S_3 micro-flowers, the absorption edge was substantially extended to a longer wavelength, and an enhanced absorption intensity in the visible light region was clearly observed (Figure 6b). Thus, 3D MoS_2/Bi_2S_3 could be excited to generate many more electron-hole pairs under visible light irradiation, possibly leading to an enhanced photocatalytic activity for pollutant degradation. In addition, the favorable electronic coupling for the rapid electron transport from the less conductive Bi_2S_3 micro-flowers to the more conductive MoS_2 nanosheets in 3D MoS_2/Bi_2S_3 (Figure 6c) confirmed that the short-circuit photocurrent measured on 3D MoS_2/Bi_2S_3 had a higher intensity and a better stability than that measured on the Bi_2S_3, MoS_2 and P25 references (Figure 6d). The applied external bias, +0.447 V/NHE, was too low to generate any significant faradic anodic current from water oxidation by the oxygen evolution reaction (as confirmed by the rather low dark current in Figure 6d), and $E^0_{H2O/O2} = +1.23$ V/NHE. Thus, the measured photocurrents on the 3D MoS_2/Bi_2S_3 hybrid and its Bi_2S_3, MoS_2 and P25 references were mostly ascribed to the efficient generation, separation and transfer of the photo-generated electron-hole pairs under visible light irradiation ($\lambda > 420$ nm), as described by the model of hole injection into the aqueous electrolyte and electron injection into the underlying substrate and ultimately to the counter electrode. Thus, the higher and more stable photocurrent measured on 3D MoS_2/Bi_2S_3 indicates its higher generation, separation and transfer efficiency of reactive photocarriers under visible light irradiation. In principle, the superior photochemical, electrochemical and photo-electrochemical properties of the 3D MoS_2/Bi_2S_3 could favor the largest amount of photo-generated ·OH (Supplementary Figures S20a–d) and the highest photocatalytic activity for the degradation of refractory pollutants, such as RhB and atrazine (Figures 5a and b).

CONCLUSIONS

In summary, we developed a facile and general hydrothermal method to prepare a novel 3D flower-like MoS_2/Bi_2S_3 heterostructure and to simultaneously tune the layers of MoS_2 cocatalysts. With this method, Bi_2S_3 was first generated, which then acted as the sacrificial template for localized MoS_2 formation via a cation-exchange mechanism. The 3D MoS_2/Bi_2S_3 exhibited a strong adsorption capacity and excellent photocatalytic activity toward the degradation of both RhB and atrazine. These findings are important for the development of novel S-based photocatalyst hybrids, for example, Sb_2S_3/MoS_2, for various environmental and energy applications.

CONFLICT OF INTEREST

The authors declare no conflict of interest.

ACKNOWLEDGEMENTS

We thank the National Science Foundation of China (51208488, 21261160489 and 51538011) and the Program for Changjiang Scholars and Innovative Research Team in University of the Ministry of Education of China for the support of this work.

Author contributions: A.-Y.Z. and H.-Q.Y. conceived the idea. L.-L.L., A.-Y.Z., Q.R., X.Z. and Y.-X.H. planned and performed the experiments and collected and analyzed the data. J.-J.C. performed the DFT calculations. L.-L.L., A.-Y.Z. and H.-Q.Y. co-wrote the manuscript. All authors discussed the results and commented on the manuscript.

1 Kershaw, S. V., Susha, A. S. & Rogach, A. L. Narrow bandgap colloidal metal chalcogenide quantum dots: synthetic methods, heterostructures, assemblies, electronic and infrared optical properties. *Chem. Soc. Rev.* **42**, 3033–3087 (2013).
2 Rhee, J. H., Chung, C. C. & Diau, W. G. A perspective of mesoscopic solar cells based on metal chalcogenide quantum dots and organometal-halide perovskites. *NPG Asia Mater.* **5**, e68 (2013).
3 Kong, D., Cha, J. J., Wang, H., Lee, H. R. & Cui, Y. First-row transition metal dichalcogenide catalysts for hydrogen evolution reaction. *Energy Environ. Sci.* **6**, 3553–3558 (2013).
4 Gao, X., Wu, H. B., Zhang, L., Zhong, Y., Hu, Y. & Lou, X. W. Formation of mesoporous heterostructured $BiVO_4/Bi_2S_3$ hollow discoids with enhanced photoactivity. *Angew. Chem. Int. Ed.* **53**, 5917–5921 (2014).
5 Li, L., Sun, L. J., Huang, Y. Y., Qin, Y., Zhao, N. N., Gao, J. N., Li, M. X., Zhou, H. H. & Qi, L. M. Topotactic transformation of single-crystalline precursor discs into disc-like Bi_2S_3 nanorod networks. *Adv. Funct. Mater.* **18**, 1194–1201 (2008).
6 Liu, Y., Yu, Y. X. & Zhang, W. D. MoS_2/CdS heterojunction with high photoelectrochemical activity for H_2 evolution under visible light: the role of MoS_2. *J. Phys. Chem. C* **117**, 12949–12957 (2013).
7 Liu, Z. Q., Huang, W. Y., Zhang, Y. M. & Tong, Y. X. Facile hydrothermal synthesis of Bi_2S_3 spheres and CuS/Bi_2S_3 composites nanostructures with enhanced visible-light photocatalytic performances. *CrystEngComm.* **14**, 8261–8267 (2012).
8 Narayanan, R., Deepa, M., Friebel, F. & Srivastava, A. K. A CdS/Bi_2S_3 bilayer and a poly (3,4-ethylenedioxythiophene)/S_2 interface control quantum dot solar cell performance. *Electrochim. Acta* **105**, 599–611 (2013).
9 Fang, Z., Liu, Y. F., Fan, Y. T., Ni, Y. H., Wei, X. W., Tang, K. B., Shen, J. M. & Chen, Y. Epitaxial growth of CdS nanoparticle on Bi_2S_3 nanowire and photocatalytic application of the heterostructure. *J. Phys. Chem. C* **115**, 13968–13976 (2011).
10 Wu, Z., Chen, L., Xing, C., Jiang, D., Xie, J. & Chen, M. Controlled synthesis of Bi_2S_3/ZnS microspheres by an in situ ion-exchange process with enhanced visible light photocatalytic activity. *Dalton Trans.* **42**, 12980–12988 (2013).
11 He, H., Berglund, Sean, P., Xiao, P. & Chemelewski, W. D. Nanostructured Bi_2S_3/WO_3 heterojunction films exhibiting enhanced photoelectrochemical performance. *J. Mater. Chem. A* **1**, 12826–12834 (2013).
12 Tan, C. & Zhang, H. Two-dimensional transition metal dichalcogenide nanosheet-based composites. *Chem. Soc. Rev.* **44**, 2713–2731 (2015).

13 Huang, X., Zeng, Z. & Zhang, H. Metal dichalcogenide nanosheets: preparation, properties and applications. *Chem. Soc. Rev.* **42**, 1934–1946 (2013).
14 Zhang, X. & Xie, Y. Recent advances in free-standing two-dimensional crystals with atomic thickness: design, assembly and transfer strategies. *Chem. Soc. Rev.* **42**, 8187–8199 (2013).
15 Karunadasa, H. I., Montalvo, E., Sun, Y. J., Majda, M., Long, J. R. & Chang, C. J. A molecular MoS_2 edge site mimic for catalytic hydrogen generation. *Science* **335**, 698–702 (2012).
16 Chang, K., Mei, Z. W., Wang, T., Kang, Q., Yang, S. X. & Ye, J. H. MoS_2/Graphene cocatalyst for efficient photocatalytic H_2 evolution under visible light irradiation. *ACS Nano* **8**, 7078–7087 (2014).
17 Wan, Z., Yin, Z., Du, Y., Huang, X., Zeng, Z., Fan, Z., Liu, H., Wang, J. & Zhang, H. Core-shell structure of hierarchical quasi-hollow MoS_2 microspheres encapsulated porous carbon as stable anode for Li-ion batteries. *Small* **10**, 4975–4981 (2014).
18 Kibsgaard, J., Chen, Z., Reinecked, B. & Jaramillo, T. F. Engineering the surface structure of MoS_2 to preferentially expose active edge sites for electrocatalysis. *Nat. Mater.* **11**, 963–969 (2012).
19 Weng, B., Zhang, X., Zhang, N., Tang, Z. R. & Xu, Y. J. Two-dimensional MoS_2 nanosheet-coated Bi_2S_3 discoids: synthesis, formation mechanism, and photocatalytic application. *Langmuir* **31**, 4314–4322 (2015).
20 Wang, S., Li, X., Chen, Y., Cai, X., Yao, H., Gao, W., Zheng, Y., An, X., Shi, J. & Chen, H. A facile one-pot synthesis of a two-dimensional MoS_2/Bi_2S_3 composite theranostic nanosystem for multi-modality tumor imaging and therapy. *Adv. Mater.* **17**, 2775–2782 (2015).
21 Xiang, Q., Yu, J. G. & Jaroniec, M. Synergetic effect of MoS_2 and graphene as cocatalysts for enhanced photocatalytic H_2 production activity of TiO_2 nanoparticles. *J. Am. Chem. Soc.* **134**, 6575–6578 (2012).
22 Liu, M., Li, F., Sun, Z., Ma, L., Xu, L. & Wang, Y. Noble-metal-free photocatalysts MoS_2-graphene/CdS mixed nanoparticles/nanorods morphology with high visible light efficiency for H_2 evolution. *Chem. Commun.* **50**, 11004–11007 (2014).
23 Jia, T. T., Kolpin, A., Ma, C. S., Chan, R. C.-T., Kwok, W.-M. & Tsang, S. C. E. A graphene dispersed CdS-MoS_2 nanocrystal ensemble for cooperative photocatalytic hydrogen production from water. *Chem. Commun.* **50**, 1185–1188 (2014).
24 Lang, D., Shen, T. & Xiang, Q. Roles of MoS_2 and graphene as cocatalysts in the enhanced visible-light photocatalytic H_2 production activity of multiarmed CdS nanorods. *ChemCatChem.* **7**, 943–951 (2015).
25 Li, Y. G., Wang, H. L., Xie, L. M., Liang, Y. Y., Hong, G. S. & Dai, H. J. MoS_2 nanoparticles grown on graphene: an advanced catalyst for the hydrogen evolution reaction. *J. Am. Chem. Soc.* **133**, 7296–7299 (2011).
26 Zong, X., Yan, H. J., Wu, G. P., Ma, G. J., Wen, F. Y., Wang, L. & Li, C. Enhancement of photocatalytic H_2 evolution on CdS by loading MoS_2 as cocatalyst under visible light irradiation. *J. Am. Chem. Soc.* **130**, 7176–7177 (2008).
27 Ding, S., Zhang, D., Chen, J. S. & Lou, X. W. Facile synthesis of hierarchical MoS_2 microspheres composed of few-layered nanosheets and their lithium storage properties. *Nanoscale* **4**, 95–98 (2012).
28 Zhou, W., Yin, Z., Du, Y., Huang, X., Zeng, Z., Fan, Z., Liu, H., Wang, J. & Zhang, H. Synthesis of few-layer MoS_2 nanosheet-coated TiO_2 nanobelt heterostructures for enhanced photocatalytic activities. *Small* **9**, 140–147 (2013).
29 Seo, B., Jung, G. Y., Sa, Y. J., Jeong, H. Y., Cheon, J. Y., Lee, J. H., Kim, H. Y., Kim, J. C., Shin, H. S., Kwak, S. K. & Joo, S. H. Monolayer-precision synthesis of molybdenum sulfide nanoparticles and their nanoscale size effects in the hydrogen evolution reaction. *ACS Nano* **9**, 3728–3739 (2015).
30 Chen, J., Wu, X. J., Yin, L., Li, B., Hong, X., Fan, Z., Chen, B., Xue, C. & Zhang, H. One-pot synthesis of CdS nanocrystals hybridized with single-layer transition-metal dichalcogenide nanosheets for efficient photocatalytic hydrogen evolution. *Angew. Chem. Int. Ed.* **54**, 1210–1214 (2015).
31 Wang, J., Liu, J., Chao, D., Yan, J., Lin, J. & Shen, Z. X. Self-assembly of honeycomb-like MoS_2 nanoarchitectures anchored into graphene foam for enhanced lithium-ion storage. *Adv. Mater.* **26**, 7162–7169 (2014).
32 Wang, P. P., Sun, H., Ji, Y., Li, W. & Wang, X. Three-dimensional assembly of single-layered MoS_2. *Adv. Mater.* **26**, 964–969 (2014).
33 Zhou, F., Xin, S., Liang, H. W., Song, L. T. & Yu, S. H. Carbon nanofibers decorated with molybdenum disulfide nanosheets: synergistic lithium storage and enhanced electrochemical performance. *Angew. Chem. Int. Ed.* **53**, 11552–11556 (2014).
34 Yang, L., Wang, S., Mao, J., Deng, J., Gao, Q., Tang, Y. & Schmidt, O. G. Hierarchical MoS_2/polyaniline nanowires with excellent electrochemical performance for lithium-ion batteries. *Adv. Mater.* **25**, 1180–1184 (2013).
35 Chou, S. S., De, M., Kim, J., Byun, S., Dykstra, C., Yu, J., Huang, J. & Dravid, V. P. Ligand conjugation of chemically exfoliated MoS_2. *J. Am. Chem. Soc.* **135**, 4584–4587 (2013).
36 Knoxville, T. N. & John, A. D. Lange's Handbook of Chemistry. 15th edition, 8.24-8.72 (McGraw-Hill, New York City, NY, USA, 1999).
37 Lisicki, N. M. & Böltz, D. F. UV spectrophotometric determination of bismuth by iodide and thiourea. *Anal. Chem.* **27**, 1722–1724 (1955).
38 Ivanova, E., Yan, X. P. & Adams, F. Determination of bismuth in cod muscle, lake and river sediment by flow injection on-line sorption preconcentration in a knotted reactor coupled with electrothermal atomic absorption spectrometry. *Anal. Chim. Acta* **354**, 7–13 (1997).
39 Tang, Z., Wang, Y., Shanbhag, S. & Kotov, N. A. Spontaneous CdTe→ alloy→ CdS transition of stabilizer-depleted CdTe nanoparticles induced by EDTA. *J. Am. Chem. Soc.* **128**, 7036–7042 (2006).
40 Liu, Y. H., Wang, F., Hoy, J., Wayman, V. L., Steinberg, L. K., Loomis, R. A. & Buhro, W. E. Bright core-shell semiconductor quantum wires. *J. Am. Chem. Soc.* **134**, 18797–18803 (2012).
41 Gao, Y. W., Wang, Y. & Zhang, H. Removal of Rhodamine B with Fe-supported bentonite as heterogeneous photo-Fenton catalyst under visible irradiation. *Appl. Catal. B* **178**, 29–36 (2015).
42 Xu, X., Hu, L. F., Gao, N., Liu, S. X., Wageh, S., Alghamdi, A., Alshahrie, A. & Fang, X. S. Controlled growth from ZnS nanoparticles to ZnS-CdS nanoparticle hybrids with enhanced photoactivity. *Adv. Funct. Mater.* **25**, 445–454 (2015).
43 Zhang, X., Wang, X. B., Wang, L. W., Wang, W. K., Long, L. L., Li, W. W. & Yu, H. Q. Synthesis of a highly efficient BiOCl single-crystal nanodisk photocatalyst with exposing {001} facets. *ACS Appl. Mater. Interfaces* **6**, 7766–7772 (2014).
44 Pan, C., Xu, J., Wang, Y., Li, D. & Zhu, Y. Dramatic activity of $C_3N_4/BiPO_4$ photocatalyst with core/shell structure formed by self-assembly. *Adv. Funct. Mater.* **22**, 1518–1524 (2012).
45 Gai, K., Shi, B. Y., Yan, X. M. & Wang, D. S. Effect of dispersion on adsorption of atrazine by aqueous suspensions of fullerenes. *Environ. Sci. Technol.* **45**, 5959–5965 (2011).
46 Long, L. L., Zhang, A. Y., Huang, Y. X., Zhang, X. & Yu, H. Q. A robust cocatalyst Pd_4S uniformly anchored onto Bi_2S_3 nanorods for enhanced visible light photocatalysis. *J. Mater. Chem. A* **3**, 4301–4306 (2015).
47 Chen, S., Shen, S., Liu, G., Qi, Y., Zhang, F. & Li, C. Interface engineering of a CoO_x/Ta_3N_5 photocatalyst for unprecedented water oxidation performance under visible-light-irradiation. *Angew. Chem. Int. Ed.* **54**, 3047–3051 (2015).

Supplementary Information accompanies the paper on the NPG Asia Materials website (http://www.nature.com/am)